Model-Based 3-D X-Ray Induced Acoustic Computerized Tomography

Prabodh Kumar Pandey, Siqi Wang, Leshan Sun, Lei Xing, and Liangzhong Xiang

***Abstract*—X-ray-induced acoustic (XA) computerized tomography (XACT) is an evolving imaging technique that aims to reconstruct the X-ray energy deposition from XA measurements. Main challenges in XACT are the poor signal-to-noise ratio and limited field-of-view, which cause artifacts in the images. We demonstrate the efficacy of model-based (MB) algorithms for 3-D XACT and compare with the traditional algorithms. The MB algorithms are based on the matrix free approach for regularized-least-squares minimization corresponding to XACT. The matrix-free-LSQR (MF-LSQR) and the noniterative model-backprojection (MBP) reconstructions were evaluated and compared with universal backprojection (UBP), time-reversal (TR), and fast-Fourier transform (FFT)-based reconstructions for numerical and experimental XACT datasets. The results demonstrate the capability of the MF-LSQR algorithm to reduce noisy artifacts thus yielding better reconstructions. MBP and MF-LSQR algorithms perform particularly well with the experimental XACT dataset, where noise in signals significantly affects the reconstruction of the target in UBP and FFT-based reconstructions. The TR reconstruction for experimental XACT is comparable to MF-LSQR, but takes thrice as much time and filters the frequency components greater than maximum frequency supported by the grid, resulting loss of resolution. The MB algorithms are able to overcome the challenges in XACT and hence are vital for the clinical translation of XACT.**

***Index Terms*—Biomedical imaging, least-squares (LS) problem, model back-projection, model-based (MB) image reconstruction, regularization, X-ray induced acoustic tomography (XACT).**

Manuscript received 19 July 2022; revised 31 October 2022; accepted 15 January 2023. Date of publication 19 January 2023; date of current version 3 May 2023. This work was supported in part by the National Institute of Health under Grant R37CA240806; in part by the American Cancer Society under Grant 133697-RSG-19-110-01-CCE; and in part by the UCI Chao Family Comprehensive Cancer Center under Grant P30CA062203. *(Corresponding authors: Liangzhong Xiang; Prabodh Kumar Pandey.)*

This work did not involve human subjects or animals in its research.

Prabodh Kumar Pandey is with the Department of Radiological Sciences, University of California, Irvine, CA 92697 USA (e-mail: pkpandey@hs.uci.edu).

Siqi Wang and Leshan Sun are with the Department of Biomedical Engineering, University of California, Irvine, CA 92617 USA (e-mail: s.wang@uci.edu; leshans@uci.edu).

Lei Xing is with the Division of Medical Physics, Department of Radiation Oncology, Stanford University School of Medicine, Stanford, CA 94305 USA (e-mail: lei@stanford.edu).

Liangzhong Xiang is with the Department of Radiological Sciences, the Department of Biomedical Engineering, and the Beckman Laser Institute, University of California at Irvine, Irvine, CA 92612 USA (e-mail: liangzhx@hs.uci.edu).

This article has supplementary material provided by the authors and color versions of one or more figures available at https://doi.org/10.1109/TRPMS.2023.3238017.

Digital Object Identifier 10.1109/TRPMS.2023.3238017

I. Introduction

X-RAYS are one of the widely used tools in clinics these days, commonly employed for imaging the body to investigate the structures of the internal organs [1], [2], [3], as well as for radiotherapy for treating tumors by guiding intense X-ray beams toward the tumor to destroy the malignant cells [4], [5]. X-rays, being ionizing radiation, are known to be carcinogenic [6], and hence, techniques for X-ray-based medical procedures which minimize the radiation exposure are desirable. Computed tomographic scans (commonly known as CT scans) [1], [2], [3] are very commonly used in clinics to obtain 3-D images of the organ/region of interest (ROI) in the body. This is achieved by rotating the X-rays and detectors around the body and collecting multiple projection datasets. X-ray-induced acoustic computerized tomography (XACT) is a modernistic imaging technique that aims to reconstruct the X-ray energy deposition (XED) map from boundary X-ray-induced acoustic (XA) measurements.

Absorption of pulsed X-ray radiation in tissues leads to thermoelastic expansion which produces XA waves [7]. These waves can be sensed by ultrasonic transducers around the irradiated ROI and fed to an XACT algorithm to reconstruct the XED in the ROI. Propagation of acoustic waves is inherently a 3-D phenomenon, and hence unlike CT scans, XACT can potentially facilitate 3-D imaging from XA measurements obtained from X-ray excitation from one direction, thereby reducing the radiation exposure. Lower scattering of X-rays and XA waves in tissues enables XACT [7], [8], [9], [10], [11], [12], [13], [14], [15], [16], [17], [18], [19], [20], [21], [22], [23], [24], [25], [26], [27] to image deeper in the body. The potential clinical applications XACT is currently being researched for are dose-monitoring during radiotherapy [11], [12] and tomographic imaging [13], [14].

XACT was first demonstrated by Xiang et al. [7], where a chicken tissue with targets embedded was irradiated with X-ray pulses and the XA signals were collected by rotating a transducer element around the tissue. The backprojection (BP) algorithm was employed to evaluate 2-D reconstructions showing the embedded targets. Over the past ten years, researchers have explored several potential tomographic imaging applications of XACT, such as imaging microcalcifications for breast cancer diagnosis [14], imaging tumors using fiducial markers [15], and bone imaging [16]. XACT using a synchrotron-based X-ray source was demonstrated in [17] which overcomes the limitations of the traditionally used X-ray sources, such as portable tubes and the linear accelerators

(Linac). Typically, XACT signals require multiple averaging and hence higher radiation exposure and scanning time. In a recent publication [18], we demonstrated the capability of 2-D XACT reconstruction from ring array measurements with a single pulse excitation of the sample. One of the bottlenecks for in vivo XACT imaging in clinics is the poor SNR of the XA signals. Choi et al. [19] demonstrated in situ XACT using Gastrografin, a conventional CT contrast agent which improved the SNR of the XA signals.

Radiation dosimetry is another application that XACT researchers across the globe have delved into. The XED and hence the strength of the collected XA signals are directly proportional to the deposited dose in the tissue. Several articles [11], [20], [21], [22], [23] discuss computational studies (both in 2-D and 3-D) exploring the feasibility of radiation dosimetry using XACT. The early experimental studies demonstrated 2-D maps of the XED by Linac X-ray pulse in water [24], [25] and veal liver tissue [26]. Kim et al. [12], [27] demonstrated the capability of dose monitoring in 3-D by scanning a spherically focused transducer element along a line at multiple depths. All these numerical and experimental studies indicate the potential of XACT for medical imaging and dosimetry. Clinical X-rays have been demonstrated to produce reasonable XA signal strength and XA measurements can easily be carried out in clinics by integrating a coupling medium and ultrasonic detection grid.

The XACT setups in many of the aforementioned studies use a single-element transducer for detecting the XA signals. Such transducers have larger aperture size and hence the collected XA signals have reasonable SNRs. However, data collection for imaging purposes needs the transducer to be scanned around the ROI thus increasing the acquisition time and the radiation exposure. To overcome this drawback, XACT can employ a detection array of small transducer elements facilitating multichannel data acquisition (DAQ), but at the cost of decreased SNR.

The inverse problem corresponding to XACT is to reconstruct the XED map in an ROI from the XA signals collected at various spatial locations around the ROI. This is traditionally achieved using the BP algorithms [28]. BP algorithms, though computationally efficient, carry certain drawbacks, such as limited view, and noisy artifacts for low SNR XA data. Model-based (MB) algorithms on the other hand, not only ameliorate these artifacts but can also facilitate incorporating experimental attributes, such as acoustic inhomogeneity, finite detector size, etc. In our recent article [29], we demonstrated the first MB, 2-D XACT reconstructions from ring-array measurements. We also demonstrated how MB reconstructions can diminish the ring artifacts which occur because of the nonuniform response among the detectors as a result of the interference between the multichannel DAQ electronics [30]. In this work, we demonstrate MB 3-D XACT reconstructions and compare them with the traditional reconstructions. The MB reconstruction algorithm employed in this work is first validated on the numerical measurements generated using the k-wave toolbox [31] in spherical and planar detection geometries and then used to reconstruct a lead target from experimental XACT measurements. This we believe is the first illustration of 3-D XACT using the MB algorithm.

The physics of XACT is similar to that of photoacoustic or optoacoustic tomography (PAT/OAT) [28]. The main difference between these two modalities is that XACT employs X-ray radiation and aims to image the X-ray absorption-based contrast, while PAT relies on optical radiation ($\sim$ hundreds of nanometers wavelengths) and images the optical absorption contrast in the ROI. The penetration depth of PAT is limited to a few centimeters due to high optical scattering in tissues. X-rays on the other hand penetrate much deeper and high energy X-rays can penetrate through the human body. Due to the shallow penetration depths, PAT is typically used for imaging soft tissues where the variation in sound speed is very small (<10%) [32]. XACT on the other hand can have bones within the ROI where the sound speed is about twice of that in water and soft tissues [32]. Moreover, PAT typically uses lasers with nanosecond pulse duration as the source while the commonly used X-ray sources such as LINACs typically have a pulsewidth of several microseconds. The shorter pulse duration in PAT facilitates higher photoacoustic efficiency as well as higher frequency content in the acoustic signals and hence high-resolution imaging. XACT signals on the other hand typically have lower SNRs and frequency content. The high penetration depth of XACT also contributes toward lowering the frequency content of the XA signals because the higher frequency components of the XA waves originating deep in the tissue are strongly attenuated. These drawbacks of XACT with respect to PAT motivate the need for superior image reconstruction algorithms than the backprojection-based ones, which are commonly employed in XACT. One of the applications that XACT is being researched for is radiation dosimetry which seeks a quantitative XED map in the organ being treat during radiotherapy. This further emphasizes the need for advanced image reconstruction algorithms which can facilitate quantitative imaging.

MB reconstruction schemes are based upon a model that relates the XED with the XA signals measured at detectors and XACT can borrow the model used in PAT, a sister modality that shares similar physics. MB reconstruction algorithms have been reported to be very successful in PAT and a detailed review of the 3-D PAT models and corresponding reconstruction algorithms can be found in [33]. Here, we limit our discussion to discrete-to-discrete (D-D) forward models with homogeneous sound speed, negligible acoustic attenuation, and point detector assumptions. PAT forward model is inherently a continuous-to-discrete (C-D) mapping because the photoacoustic measurements are discrete while the optical energy deposition (pressure source) is continuous. To be able to employ the model in optimization-based tomographic inversion, an equivalent D-D mapping is desired. To achieve this, the heat/pressure source map $H(\vec{r})$ needs to be represented in the discrete domain: $H(\vec{r}) \equiv \underline{h}$. This is achieved by using expansion functions that define the variation of the pressure source in each discrete element. Kaiser–Bessel (KB) window functions [34], [35], [36] and linear interpolation functions [37], [38], [39], [40] are some of the commonly used expansion functions used in PAT.

In [29] and [30], we employed linear interpolation functions for modeling and subsequent image reconstruction in 2-D XACT. In this manuscript, we chose $H(\vec{r})$ to be constant within each voxel to avoid computing the expansion coefficients during the iterative image reconstruction algorithm. We observed that with a high angular discretization for computing the surface integral in the acoustic propagation operator (detailed later in Section II-A), our model matches reasonably well with the simulations done using the *k*-wave toolbox, a popular open source PAT toolbox [31]. All the measurements (forward data) used in the numerical studies in this article were also computed using the *k*-wave toolbox to avoid inverse crime.

The D-D forward model is typically expressed in the form: $\underline{p} = \mathbf{M}\underline{h}$, with $\mathbf{M}$ being the model matrix relating the discrete domain XA measurements $\underline{p}$ with, $\underline{h}$ the discrete domain representation of the XED. For 3-D problems as well as for problems involving high resolution and high sampling frequency, the computation and assembly of the model matrix can be time consuming and storing it can be computationally demanding. Moreover, evaluation of reconstruction commonly involves regularized inversion of $\mathbf{M}$ which further increases the computational demands [29]. In this article, we overcome these challenges by using a matrix-free (MF) approach for solving the least-squares (LS) problem (matrix-free-LSQR (MF-LSQR)) corresponding to XACT. This method employs functions for computing $\mathbf{M}\underline{u}$ and $\boldsymbol{M}^{\boldsymbol{T}}\underline{v}$ (matrix-vector multiplications) in MATLAB's LSQR (LS with QR factorization) function to iteratively compute the minimizer to the XACT LS problem. We also demonstrate a noniterative MB reconstruction (known as model-backprojection (MBP) [29], [41], [42]) which is computationally efficient, but only provides the structural information in the ROI.

In this manuscript, the theory and numerical implementation of the XACT forward model and corresponding tomographic problem are discussed in Section II. Section III deals with the computational validation of the MB reconstruction schemes and the phantom XACT experiments are described in Section IV. Concluding remarks are offered in Section V.

II. Mathematical Formulation

A. Forward Problem

Propagation of the XA waves in acoustically homogeneous and negligibly attenuating media following XED under thermal and stress confinement is governed by the wave equation [28]:

$$\frac{\partial^2 p(\vec{r},t)}{\partial t^2} - \nu^2 \nabla^2 p(\vec{r},t) = \Gamma H(\vec{r}) \frac{\partial \delta(t)}{\partial t} \tag{1}$$

with Γ, ν, and H being the Gruneisen constant, the acoustic propagation speed, and the XED map. Solution to (1) after dropping the multiplicative constant can be written as [29]:

$$p(\vec{r},t) = \frac{\partial}{\partial t}\left(\frac{1}{vt}\int_{S(\vec{r},t)} H(\vec{r}')dS'(t)\right); |\vec{r}-\vec{r}'| = vt \tag{2}$$

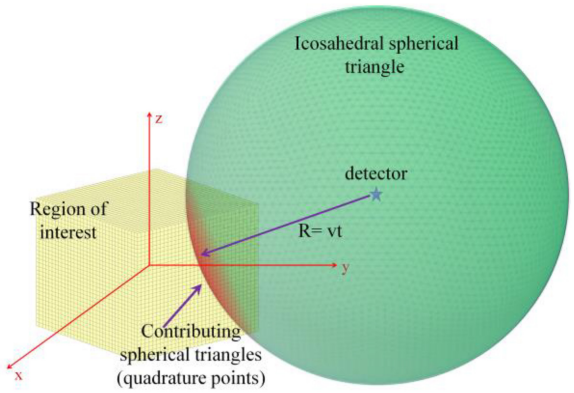

Fig. 1. Demonstration of the method for computing the surface integral in (3).

where $S(\vec{r},t)$ is a spherical surface centered at a detector (located at $\vec{r}$) such that its radius at time t is $R(t) = |\vec{r}-\vec{r}'| = vt$. Equation (2) can further be simplified to

$$p(\vec{r},t) = \frac{\partial}{\partial t}\left(\text{vt}\int_{S(\vec{r},t)} H(\vec{r}')d\Omega\right). \tag{3}$$

The ROI (commonly a cube/cuboid which contains (or is expected to contain) the $H(\vec{r})$ map) is discretized into voxels and the XED is expressed in the discrete domain as: $H(\vec{r}) \equiv \underline{h}$. The value of the XED ($h(\vec{r})$) is given by

$$h(\vec{r}) = \sum_{k=1}^{N_v} h_k N_k(\vec{r})$$
$$N_k(\vec{r}) = \begin{cases} 1, \text{ if } \vec{r} \text{ lies inside the } k\text{th voxel} \\ 0, \text{ otherwise} \end{cases} \tag{4}$$

with N_v being the number of voxels in the domain.

To compute the integration over the spherical surface $S(\vec{r},t)$ in (3), a unit sphere is first discretized into M uniformly distributed triangular spherical elements, each characterized by their centroids $\{\hat{\beta}_1, \hat{\beta}_2, \ldots, \hat{\beta}_M\}$. The co-ordinates of the quadrature points for a detector located at $\vec{r}$ and at time t are $\vec{\alpha}_i = \vec{r} + vt\hat{\beta}_i$. The elements contributing to the integral over the spherical arc in (3) are simply the $\vec{\alpha}_i$s lying inside the ROI (Fig. 1). To reduce the computational burden, $h(\vec{r})$ was considered to be constant over each contributing element [total M_e elements (say)]. Hence, the surface integral in (3) for the mth detector location ($\vec{r}_m$) and qth time instant is

$$I(\vec{r}_m, t_q) = \int_{S(\vec{r},t)} H(\vec{r}')d\Omega \approx \sum_{i=1}^{M_e} H(\vec{r}_i)\Delta\Omega_i$$
$$= \sum_{i=1}^{M_e} \Delta\Omega_i \sum_{k=1}^{N_v} h_k N_k(\vec{r}_i)$$
$$I^{(m,q)} = \sum_{i=1}^{M_e} \Delta\Omega_i \, h_k^i \tag{5}$$

where $H(\vec{r}_i)$ denotes the XED at the centroid of the ith contributing quadrature element, $\Delta\Omega_i$ is the solid angle this element subtends at $\vec{r}_m$, and h_k^i denotes the XED value at the

voxel that contains $\vec{r}_i$. Equation (5) can further be expressed as follows:

$$I^{(m,q)} = \underline{v}^{(m,q)^T}\underline{h}; \quad \underline{h} = [h_1, h_2, \ldots, h_N]^T \tag{6}$$

and the integrals for all the detectors at qth time instant will be

$$I^{(q)} = \mathcal{V}^{(q)}; \quad \mathcal{V}^{(q)} = \left[\underline{v}^{(1,q)}, \underline{v}^{(2,q)}, \ldots, \underline{v}^{(N_d,q)}\right]^T. \tag{7}$$

In the same way, the $\mathcal{V}^{(q=1,\ldots,N_t)}$ can be stacked into matrix $\boldsymbol{V}$ and the integration for all the detectors at all time instances will be

$$\underline{I} = \boldsymbol{V}\underline{h}; \quad \boldsymbol{V} = \left[\mathcal{V}^{(1)^T}, \mathcal{V}^{(2)^T}, \ldots, \mathcal{V}^{(N_t)^T}\right]^T. \tag{8}$$

The differentiation in (3) can be written as:

$$\begin{aligned} p(\vec{r}, t) &= \frac{\partial}{\partial t}\big[vtI(\vec{r}, t)\big] = vt\frac{\partial}{\partial t}I(\vec{r}, t) + vI(\vec{r}, t) \\ &\approx vI(\vec{r}, t) + vt\frac{I(\vec{r}, t + \Delta t) - I(\vec{r}, t)}{\Delta t}. \end{aligned} \tag{9}$$

The XA measurements at all the detectors at the qth time step, can thus be written as:

$$\underline{p}^{(q)} = \mathfrak{M}^{(q)}\underline{h} \tag{10}$$

where

$$\begin{aligned} \mathfrak{M}^{(q)} &= v\mathcal{V}^{(q)} + vt^{(q)}\left[\frac{\mathcal{V}^{(q+1)} - \mathcal{V}^{(q)}}{\Delta t}\right] \\ &= vq\mathcal{V}^{(q+1)} + v(1-q)\mathcal{V}^{(q)}. \end{aligned} \tag{11}$$

The full XA measurement vector $\underline{p}$ (dimension: $(N_d.N_t) \times 1$) can thus be expressed as:

$$\underline{p} = \mathbf{M}\underline{h}, \mathbf{M} = \left[\mathfrak{M}^{(1)^T}, \mathfrak{M}^{(2)^T}, \ldots, \mathfrak{M}^{(N_t)^T}\right]^T \tag{12}$$

with $\mathbf{M}$ being the model-matrix (dimension: $(N_d.N_t) \times N$).

B. Inverse Problem

Corresponding tomographic problem is to evaluate the XED map ($\underline{\hat{h}}$) in the ROI from the discrete time-domain XA data ($\underline{p}_{\text{meas}}$) collected at detectors placed around the ROI. This can be written in the form of a regularized LS minimization problem [42], [43]

$$\underline{\hat{h}} = \arg\min_{\underline{h}} ||\underline{p}_{\text{meas}} - \mathbf{M}\underline{h}||_2^2 + \lambda^2||\mathbf{R}\underline{h}||_2^2 \tag{13}$$

where $\|\cdot\|_2$ is the L^2-*norm*. $\mathbf{R}$ and λ denote the regularization matrix and the regularization parameter, respectively. In this article, we used the Laplacian regularization ($\mathbf{R}$ = Incidence matrix). Solution to (13) can be obtained by evaluating

$$\underline{\hat{h}} = \left(\mathbf{M}^T\mathbf{M} + \lambda^2\mathbf{R}^T\mathbf{R}\right)^{-1}\mathbf{M}^T\underline{p}_{\text{meas}}. \tag{14}$$

For computationally demanding reconstruction problems (with a large number of measurements or nodes in the ROI), evaluating and storing $\mathbf{M}$ needs a lot of time and memory. Therefore, evaluating the reconstructions via (14) gets unrealistic. The minimizer to (13) can also be evaluated using the iterative LSQR method which utilizes direct computations of $\mathbf{M}\underline{u}$ and $\mathbf{M}^\mathbf{T}\underline{v}$, instead of using $\mathbf{M}$ explicitly.

Algorithm 1 MF Evaluation of $\mathbf{M}\underline{u}$

procedure Computing $\underline{p} = \mathbf{M}\underline{u}$;
  $\underline{p} = []$ (initialize)
  for $m = 1$ to N_d **do**
    for $q = 1$ to N_t **do**
      $\vec{\alpha}_i \leftarrow \vec{r} + \text{vq}\Delta t\hat{\beta}_i$
      find $\vec{\alpha}_{\text{ix}}\big| < \frac{x_0}{2}\&|\vec{\alpha}_{iy}| < \frac{y_0}{2}\&|\vec{\alpha}_{iz}| < \frac{z_0}{2}$
      find the voxels in which each $\vec{\alpha}_i$ lies in:
      say voxel k (=1,2,...,n) carries $l_k\vec{\alpha}_i$s
      $I_q = \sum_{k=1}^{n}\sum_{i=1}^{l_k}\Delta\Omega_i u_k$,
    end for
    $\underline{\zeta} = [I_2, 2I_3, 3I_4, \ldots, (N_t-1)I_{N_t}, 0]^T$
    $\underline{\mu} = [0, -I_2, -2I_3, -3I_4, \ldots, -(N_t-1)I_{N_t}]^T$
    $\underline{p} \leftarrow \left[\underline{p}^T, [v(\underline{\zeta} + \underline{\mu})]^T\right]^T$
  end for
  return $\underline{p}$
end procedure

Algorithm 2 MF Evaluation of $\mathbf{M}^T\underline{u}$

procedure Computing $\underline{\omega} = \mathbf{M}^T\underline{u}$;
  $\underline{\omega} = zeros(Nodes, 1)]$ (initialize)
  $\mathbf{U}$= reshape($\underline{u}, N_d \times N_t$)
  for $m = 1$ to N_d **do**
    $\underline{u}_d \leftarrow [\mathbf{U}(m, :)]^T$
    for $q = 1$ to N_t **do**
      $\vec{\alpha}_i \leftarrow \vec{r} + \text{vq}\Delta t\hat{\beta}_i$
      find $\vec{\alpha}_{ix}\big| < \frac{x_0}{2}\&|\vec{\alpha}_{iy}| < \frac{y_0}{2}\&|\vec{\alpha}_{iz}| < \frac{z_0}{2}$
      find the voxels in which each $\vec{\alpha}_i$s lie in:
      say voxel $k(= 1, 2, \ldots, n)$ carries $l_k\vec{\alpha}_i$s
      $\gamma = \underline{u}_d(q)(1-q) + \underline{u}_d(q-1)(q-1)$
      $\underline{\in} = zeros(Nodes, 1)$
      for $k = 1$ to n **do**
        $\in(k) = \gamma v\sum_{i=1}^{l_k}\Delta\Omega_i$,
      end for
      $\underline{\omega} \leftarrow \underline{\omega} + \underline{\in}$
    end for
  end for
  return $\underline{\omega}$
end procedure

The algorithms for matrix-vector multiplications: $\mathbf{M}\underline{u}$ and $\mathbf{M}^\mathbf{T}\underline{v}$ are given in Algorithms 1 and 2, respectively. We also demonstrate a noniterative, model-based back-projection (MBP) reconstruction [42], which is computed using

$$\underline{\hat{h}} = \mathbf{M}^\mathbf{T}\underline{p}_{\text{meas}}. \tag{15}$$

MBP is an approximation to (14), when, $\mathbf{M}^T\mathbf{M} \ll \lambda^2\mathbf{R}^T\mathbf{R}$, with $\mathbf{R} = \mathbf{I}$ (Tikhonov regularization).

III. Numerical Studies

The detection geometries as well as the phantom considered in the numerical study are depicted in Fig. 2. To perform

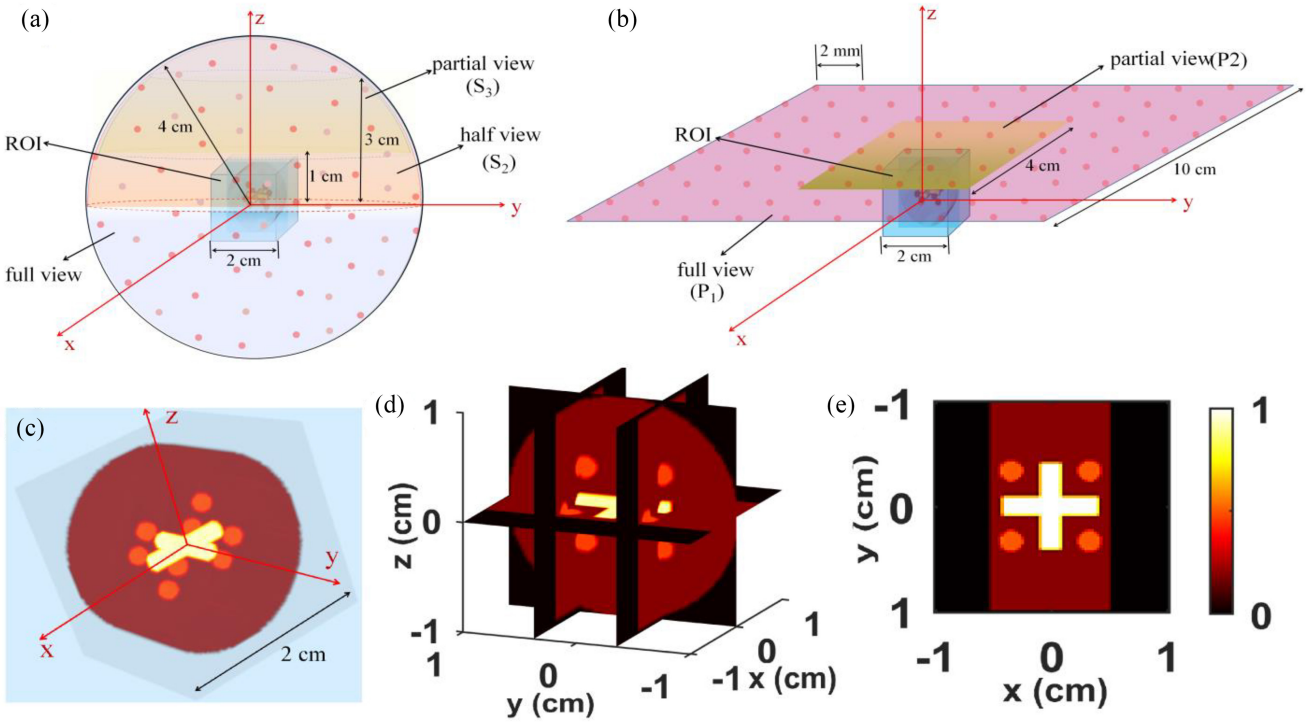

Fig. 2. Schematic of the full and partial view setting in (a) spherical and (b) planar detection geometries. (c) 3-D representation, (d) multiple slices, (e) z=0 plane slice of the phantom used in the numerical study.

the numerical validation of the developed algorithms, the numerical XA measurements were generated using the *k*-wave toolbox [31], and the algorithms for performing reconstructions were coded and executed on MATLAB R2020a. All computations were performed on a workstation with AMD Ryzen Threadripper 3960X 24-Core Processor (3.79 GHz), 256-GB installed RAM on Windows 10, 64-bit operating system.

A. Validation of the MF-LSQR Algorithms

The forward and adjoint operator evaluations $\mathbf{M}\underline{u}$ and $\mathbf{M}^{\mathbf{T}}\underline{v}$ were validated for a simple 3-D problem for which the matrix $\mathbf{M}$ could be computed and stored. In this problem, the ROI was chosen to be a cube of 1-cm edge length, discretized with 0.25-mm grid resolution ($41 \times 41 \times 41$ nodes). On the surface of a sphere of 4 cm, 80 detectors were placed, and the 106 temporal measurements for each detector were evaluated at 2-MHz sampling frequency. For this problem, the model-matrix $\mathbf{M}$ of size ($80*106 \times 41^3$) was computed and stored. The pressure source was chosen to be a sphere of radius 2.5 mm, located at the center of the ROI. The discrete-domain representation of this pressure source was chosen as $\underline{u}$. The validation of the on-the-fly $\mathbf{M}\underline{u}$ function with the explicit matrix-vector product evaluation is demonstrated in Fig. 3(a) and (b).

For the validation of the on-the-fly $\mathbf{M}^{\mathbf{T}}\underline{v}$ function, $\underline{v}$ was chosen as a random vector of size ($80*106 \times 1$) and the stem plots of the on-the-fly function and the explicit matrix-vector product $\mathbf{M}^{\mathbf{T}}\underline{v}$ evaluation is demonstrated in Fig. 3(c) and the difference between these quantities is shown in Fig. 3(d). The magnitudes of these differences are $\sim 10^{-15}$ times smaller than the values which validate the on-the-fly $\mathbf{M}^{\mathbf{T}}\underline{v}$ function.

For this problem setup, we also perform a reconstruction for the inverse crime scenario, where the measurements as well as the MF-LSQR reconstruction, both were evaluated on the same grid and using the same model without additive noise or employing regularization. Fig. 3(e) shows the convergence of the ($\log_{10}$ of the) relative residuals for 177 iterations when the relative residual decreases $<10^{-10}$.

B. Generating Measurements Using k-Wave Toolbox

As shown in Fig. 2, a cube with 2-cm edge length was chosen as the ROI, and consisted of a cross (amplitude 1) and eight spheres (amplitude 0.5) which were located in a larger cylinder (amplitude 0.2). We performed simulations for spherical as well as planar detection geometries, depicted in Fig. 2(a) and (b), respectively.

1) *Spherical Detection:* Sphere with 4-cm radius, with 1280 elements uniformly spread over the sphere (S1), upper half of the sphere ($z > 0$) with 630 detectors (S2), and a cup array with 312 detectors on the spherical surface with 1 cm $\leq z \leq$ 3 cm (S3).
2) *Planar Detection:* 10 cm $\times$ 10 cm grid (P1) and 4 cm $\times$ 4 cm grid (P2), both with 2-mm separation between each detection elements. The 3-D perspective view, multiple slices, and the $z = 0$ slice of the phantom used for the numerical validation are shown in Fig. 2(c)–(e), respectively.

The computational domain was discretized into cubical voxels (size: $h = 0.2$ mm). Such a discretization leads to the maximum supported frequency of $f_{\max} = v/2h = 3.75$ MHz. The sampling frequency has therefore been chosen to be $f_s = 10$ MHz, satisfying the Nyquist criterion ($f_s > 2f_{\max}$).

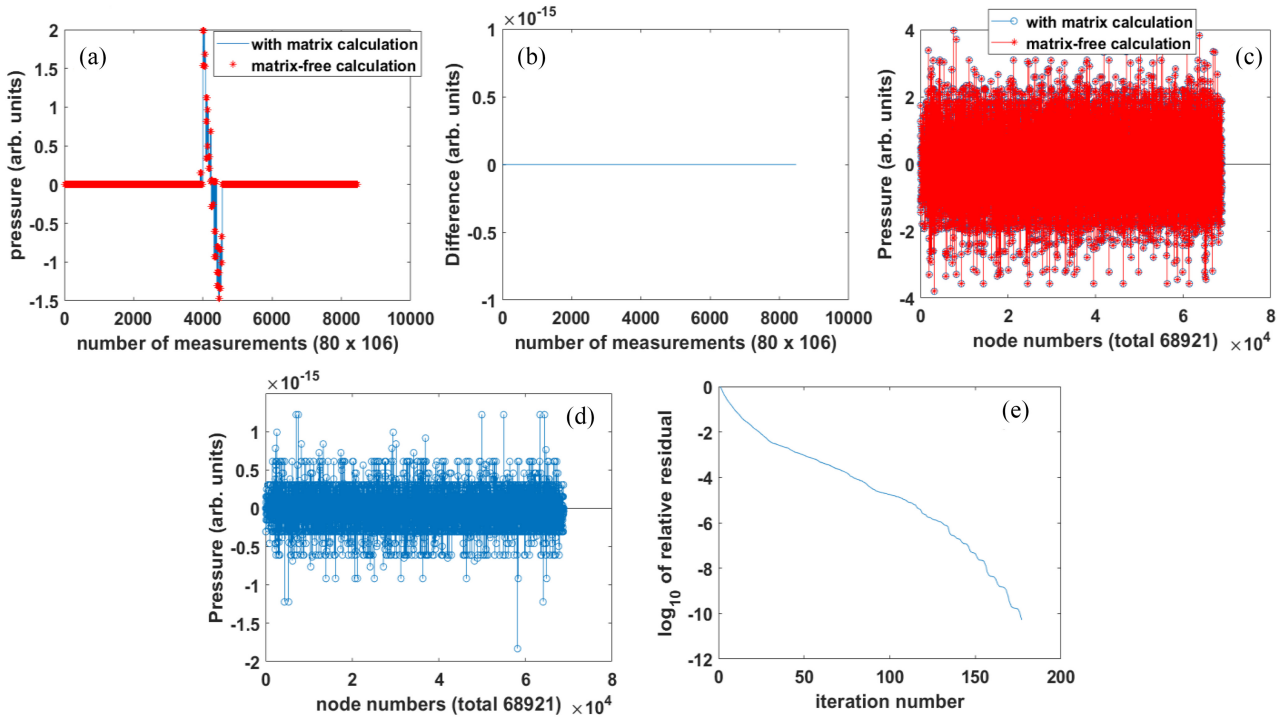

Fig. 3. (a) Pointwise matching of the model-matrix-based and on-the-fly $\mathbf{M}\underline{u}$ computation and (b) pointwise difference. Stem plots of (c) pointwise matching of the model-matrix-based and on-the-fly $\mathbf{M}^T\underline{v}$ computation and (d) pointwise difference. (e) Convergence of the relative residual with increasing iteration number for an inverse crime scenario.

The simulated signals were then contaminated with the white Gaussian noise to have 5-dB SNR in the measurements.

C. Evaluating the Reconstructions

Universal backprojection (UBP) [28], time reversal (TR) and fast Fourier-transform (FFT) based (both using the *k*-wave toolbox [31]), and the MB algorithms (MBP and Laplacian regularized MF-LSQR) were employed to evaluate the reconstructions at 0.25-mm grid resolution. The *k*-wave toolbox supports FFT-based reconstructions only for the planar detection geometry using the function *kspacePlaneRecon* for 3-D (corresponding 2-D analog is *kspaceLineRecon*). For evaluating the MB reconstructions, the unit sphere [for numerically computing the integration over the spherical arc in (3)] described in Section II-A, was discretized into $M{\sim}5{\times}10^5$ elements.

The stopping criterion and the strategy to tune the regularization parameter are essential for an iterative image reconstruction algorithm. The functional one aims to minimize [(13) in the manuscript] decreases with each LSQR iteration. The computation time for LSQR minimization is directly proportional to the number of iterations. Therefore, it is reasonable to enforce the stopping criterion when the change in the minimizers (reconstructions in our case) becomes negligible between the iterations. For the computational test cases considered in the manuscript, we observed the variation of the correlation coefficient [44] of the LSQR minimizer with respect to the solution from the previous iteration. The plot corresponding to test cases P2, S2, and S3 are provided in the supplementary material (Fig. SM1). Based on the plot we see >99.9% correlation between subsequent updates after ∼10 LSQR iterations and it also resulted reasonable reconstructions. Therefore, throughout the manuscript, we used ten iterations for evaluating the MF-LSQR reconstructions. A similar number of iterations were used for MB PAT reconstructions in [40] and [42].

The regularization parameter (λ) is typically chosen based on the tradeoff between the data fidelity $||\underline{p}_{\text{meas}} - \mathbf{M}\underline{h}||_2$ and the regularization term $||\mathbf{R}\underline{h}||_2$. In medical imaging, it is more common to choose regularization parameter that results in images that are maximally useful for specified diagnostic tasks. The L-curve method is one of the popular approaches for evaluating the regularization parameter for optimization problems [45]. L-curve plots the log of the two terms from the error functional (given in (13) in the manuscript): 1) log of the regularized solution norm ($\log(||\mathbf{R}\underline{h}||_2)$) versus 2) the log of the corresponding residual norm $\log||\underline{p}_{\text{meas}} - \mathbf{M}\underline{h}||_2$ for multiple regularization parameters (λ) with $\underline{h}$ being solutions obtained for these λs. The optimal λ is the one that corresponds to the corner of the L-curve. Therefore, the L-curve demonstrates the tradeoff between minimizing these two terms, which is the basic idea behind regularization.

As evident from its standard definition, plotting an L-curve would need computing the solution $\underline{h}$ for multiple λs, which would require high computation time and is unrealistic. Alternatively, the toolbox [45] has a function "l_curve" which takes the measurements ($\underline{p}_{\text{meas}}$) and the matrices U and s obtained from the compact form of the singular value decomposition (SVD) of the model-matrix $\mathbf{M}$, given as: $M = U{*}\text{diag}(s){*}V'$, where U is $m \times \min(m,n)$, s is $\min(m,n){\times}\ 1$, and V is $n \times \min(m,n)$. However, the algorithm presented in

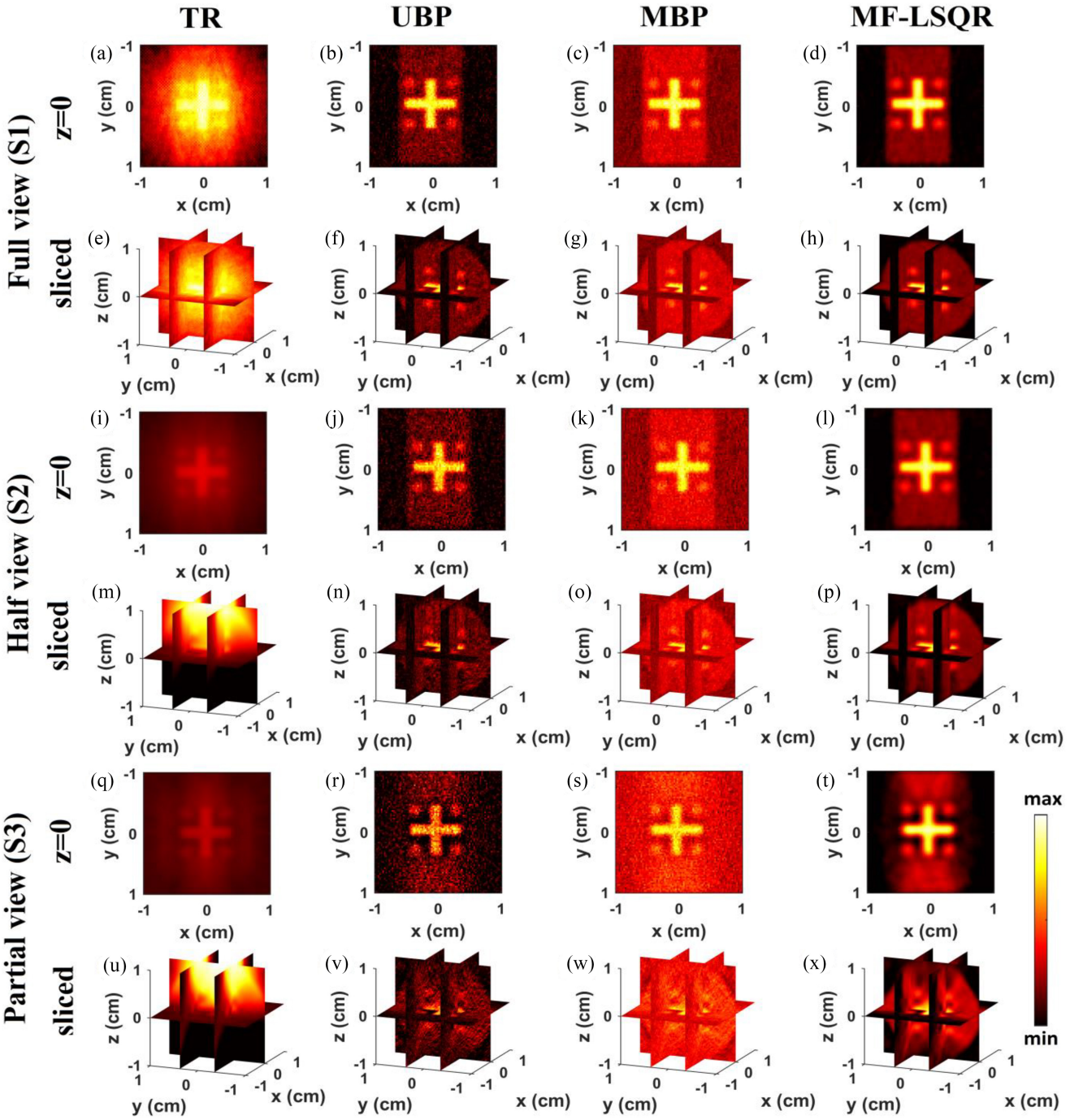

Fig. 4. Spherical geometry (S1, S2, and S3) reconstruction results. Column-I (a), (e), (i), (m), (q), and (u): TR, column-II (b), (f), (j), (n), (r), and (v): UBP, column-III (c), (g), (k), (o), (s), and (w): MBP, and column-III: (d), (h), (l), (p), (t), and (x) MF-LSQR reconstructions.

this manuscript does not compute **M** explicitly, and hence this method cannot be used for evaluating the appropriate regularization parameter. Therefore, the regularization parameters were chosen by tuning based on our computational experience. Future research will focus on the efficient evaluation of an appropriate regularization parameter for MF-LSQR-based XACT reconstruction.

D. Reconstruction Results

The TR, FFT, UBP, MBP, and MF-LSQR reconstructions of the phantom obtained from the spherical and planar detection geometries [Fig. 2(a) and (b)] are demonstrated in Figs. 4 and 5, respectively. The time taken for computing the reconstructions (τ) and the correlation coefficients (ρ) [44] w.r.t. the original phantom are tabulated in Table I. As expected, both the back-projection algorithms (UBP and MBP) and the FFT-based algorithm, being noniterative in nature, are more efficient in evaluating the reconstructions than the MF-LSQR algorithm. The TR algorithm takes the longest for evaluating the reconstructions because it needs to evaluate wave-propagation for each time step. The structures in the cross-section are reasonably reconstructed for

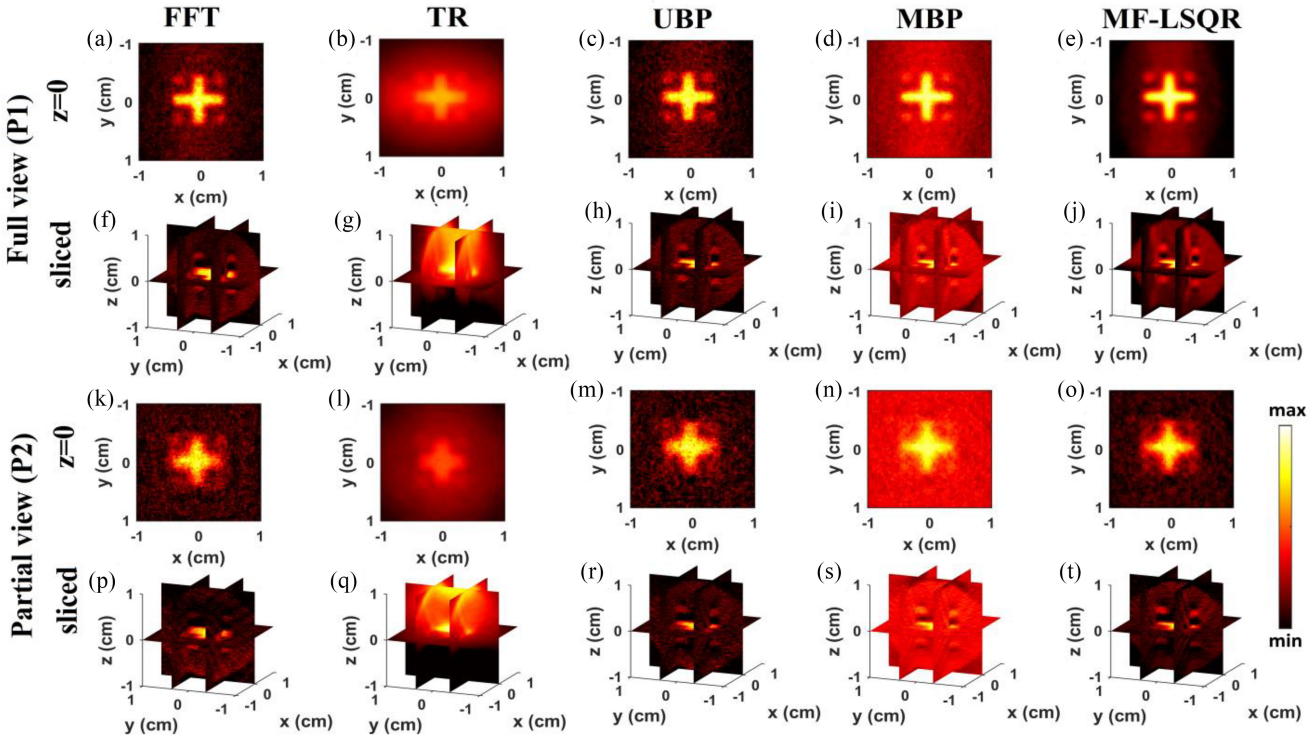

Fig. 5. Planar geometry (P1 and P2) reconstruction results. Column-I: (a), (f), (k), and (p) FFT based, Column-II: (b), (g), (l), and (q) TR, Column-III: (c), (h), (m), and (r) UBP, column-IV: (d), (i), (n), and (s) MBP, and column-V: (e), (j), (o), and (t) MF-LSQR reconstructions.

TABLE I
COMPUTATION TIME (τ) AND CORRELATION COEFFICIENT (ρ) FOR NUMERICAL STUDIES

View	Spherical Geometry								View	Planar Geometry									
	TR		UBP		MBP		MF-LSQR			FFT		TR		UBP		MBP		MF-LSQR	
	ρ	τ(s)	ρ	τ(s)	ρ	τ(s)	ρ	τ(s)		ρ	τ(s)	ρ	τ(s)	ρ	τ(s)	ρ	τ(s)	ρ	τ(s)
S1	0.59	952	0.78	4.6	0.83	81	0.92	873	**P1**	0.58	13	0.20	2714	0.66	8.9	0.74	173	0.82	1971
S2	0.30	937	0.68	2.5	0.74	40	0.90	436	**P2**	0.37	2.3	0.41	763	0.44	1.7	0.46	39	0.52	570
S3	0.25	944	0.48	1.5	0.56	21	0.79	236											

all the algorithms. However, the UBP and FFT reconstructions carry strong noisy artifacts which are further amplified in the limited view settings and therefore have a lower correlation w.r.t. the original phantom. The MBP does better than the UBP and FFT in terms of suppressing the noise and hence yields relatively better correlation coefficients in comparison to the UBP. As mentioned in Section I, MBP is not a quantitative reconstruction and this is indicated in the contrasts of the reconstructed entities. For example, the background region (0.5 cm $< |x| <$ 1 cm) where the true value is 0 unit, MBP reconstructs $\sim$ 0.2 units. Similarly the contrast of the spheres and the cross w.r.t. the rectangular region (-0.5 cm $< x <$ 0.5 cm) in MBP reconstructions are $\sim$1.6 and 3, respectively; corresponding true values are 2.5 and 5, which were found to be reasonably well reconstructed by UBP and MF-LSQR as these both are quantitative reconstruction algorithms. The MF-LSQR reconstructions were evaluated with the Laplacian regularization, which assisted in ameliorating the noisy artifacts. TR reconstruction is based on the pseudospectral wave propagation [31] and restricts the frequency components higher than the maximum frequency supported by the spatial resolution ($f_{\max} = v/2h$) which for $h = 0.25$ mm resolution, comes out to be 3 MHz. This inherent low-pass filtering leads to reduced noisy artifacts in the TR reconstructions. However, it also leads to the loss of information of the edges of the target which are encoded in the high-frequency components (Fig. 4 column I and Fig. 5 column II). Moreover, the TR reconstructions were found to be highly susceptible to the limited view problem and the detector sparsity. To further support this point, the TR reconstruction for S1 geometry, with the pressure measurements interpolated all over the spherical detection surface is demonstrated in the supplementary material Fig. SM2. Across all numerical evaluations performed in the study, MF-LSQR yielded the best reconstructions and hence higher ρ values w.r.t. the TR, FFT, UBP, and MBP counterparts.

The ease of computation associated with the UBP makes it computationally most efficient. Although, MBP is also termed as "backprojection," the operator corresponding to MBP evaluation given in Algorithm 2, is computationally more involving

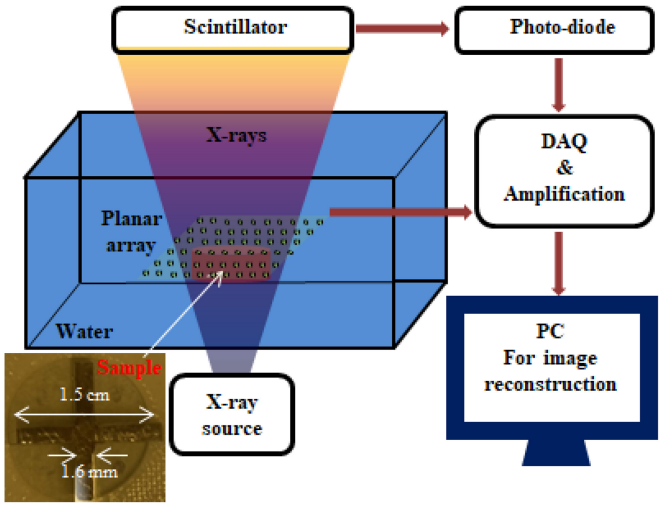

Fig. 6. Schematic of the XACT experiment.

than the UBP, and hence takes longer to compute. Moreover, at this point, while our UBP implementation has been vectorized and made efficient, improving the MB algorithms is a work in progress. We do expect to accelerate the MBP computation to achieve the performance similar to UBP. MB algrothms though computationally rigorous, offer the flexibility of incorporating regularization and experimental attributes, such as finite detector size, acoustic heterogeneity, etc. in the model and hence are desirable. As discussed in Section II-B, the MBP needs a single evaluation of $\mathbf{M}^{\mathbf{T}}\underline{v}$. The MF-LSQR is an iterative scheme and each iteration requires a $\{\mathbf{M}\underline{u}, \mathbf{M}^{\mathbf{T}}\underline{v}\}$ evaluation; $\mathbf{M}^{\mathbf{T}}\underline{v}$ being computationally more demanding. In our work, the MF-LSQR algorithm was found to converge at $\sim$ 10 iterates. Therefore, in all the test cases, MF-LSQR takes $\sim$10–15 times longer than MBP.

IV. XACT Experiment and Reconstruction

The developed MB schemes were employed to evaluate reconstructions from experimental XACT data. The schematic of the setup is depicted in Fig. 6. A "+" shaped lead target (thickness: 1/16 inch) was placed at the center of a phantom prepared using 3% agar (BactoTM, Becton, Dickinson and Company, NJ, the United States). This phantom was submersed in water and excited using a portable and battery-driven pulsed X-ray source (XR200, Golden Engineering, IN, USA) with tube energy: 150 kVp and 40° beam divergence which emits X-ray pulses with 50-ns pulse-width at 10-Hz repetition rate. The averaged dose at the target located at $\sim$ 30.5 cm from the source was estimated to be 2.6 mR/pulse for the diverging X-ray pulse. The x-ray source was shielded in a cage and was controlled through a remote from the outside. A 256-element planar array transducer (size: 4 cm $\times$ 4 cm; Doppler Electronic Technologies Company Ltd., Guangzhou, China) with 1-MHz central frequency was used to collect the XA signals. These signals were then directed to a customized 256-channel DAQ device (Legion ADC, Photosound Technologies Inc., Houston, the United States) which had a 256-channel preamplifier integrated to enhance the SNR of the XA signals. A scintillator (Ce:Lu_2SiO_5 crystal, MTI Corporation, CA, USA) was placed behind the water tank to collect the X-rays exiting the water tank. The scintillator converts the collected X-rays to visible light. The photons were then detected by an integrated variable-vain, InGaAs avalanche photodetector (APD410C, Thorlabs, NJ, USA) which sends the trigger signal to a wave generator which further relays the trigger to the Legion ADC DAQ system as square pulsed with 4-V strength for precise timing control.

TABLE II
Computation Time (τ) and CNRs (C1 and C2) for Experimental XACT Reconstructions

	FFT		TR		UBP		MBP		MF-LSQR	
	Sliced	MIP	Sliced	MIP	Sliced	MIP	Sliced	MIP	Sliced	MIP
C1	0.80	0.23	1.69	2.47	0.50	0.20	0.84	1.15	1.19	1.90
C2	0.85	0.68	3.07	3.01	0.70	0.46	1.11	1.45	1.31	2.21
τ(s)	18		2081		1.5		65		693	

The acquired experimental XA data were then used to evaluate the TR, FFT, UBP, MBP, and MF-LSQR-based XACT reconstructions. The results thus obtained are demonstrated in Fig. 7, which shows the 3-D reconstructions (first row), maximum intensity projections [(MIPs)—second row], and the reconstruction slice (at a plane 3.5-cm away from the detection grid—third row) from the TR, FFT, UBP, MBP, and MF-LSQR reconstructions, respectively. The evaluation times and contrast-to-noise ratios (CNRs) [46] are provided in Table II. The CNRs (C1 and C2) were computed for two regions in the blue and yellow rectangles, respectively, w.r.t. the background (green rectangle). The weak XACT signal is corrupted with strong noise. In addition to the low SNR, the detection geometry has a very limited view for collection. Therefore, the resolution in the reconstructed images is poor as expected. The noisy artifacts overshadow the reconstructed target in the UBP reconstructions and hence UBP reconstruction has low CNRs in the slice as well as the MIP.

The FFT-based reconstructions perform marginally better than the UBP which also reflects in the CNRs given in Table II. While the target is barely perceivable in the UBP reconstruction, it is clearly visible in both the MB and TR reconstructions, thus yielding higher CNRs as compared to the UBP. The Laplacian regularization has stronger noise ameliorating capability and hence the MF-LSQR reconstruction yields better CNRs than UBP, FFT, and MBP for the chosen regions. As mentioned earlier in Section III-D, TR reconstruction restricts the frequency components higher than the maximum frequency supported by the spatial resolution ($f_{\max} = v/2h$) which for $h = 0.25$ mm resolution, comes out to be 3 MHz. This leads to reducing the noise in the reconstructions and hence TR yields the best CNR values among all the other reconstructions. However, it also leads to the loss of information of the edges of the target which are encoded in the high-frequency components thus the resolution is adversely affected. It is evident in Fig. 8, where the reconstructed profiles [across four locations displayed by white lines in Fig. 7(o)] are compared for MF-LSQR and TR algorithms. The FWHM of these profiles were also calculated by fitting them to Gaussians and displayed in the legends of each plot. For each of the plots, the FWHMs of TR reconstructions were $\sim$15%–35% larger than the MF-LSQR counterparts.

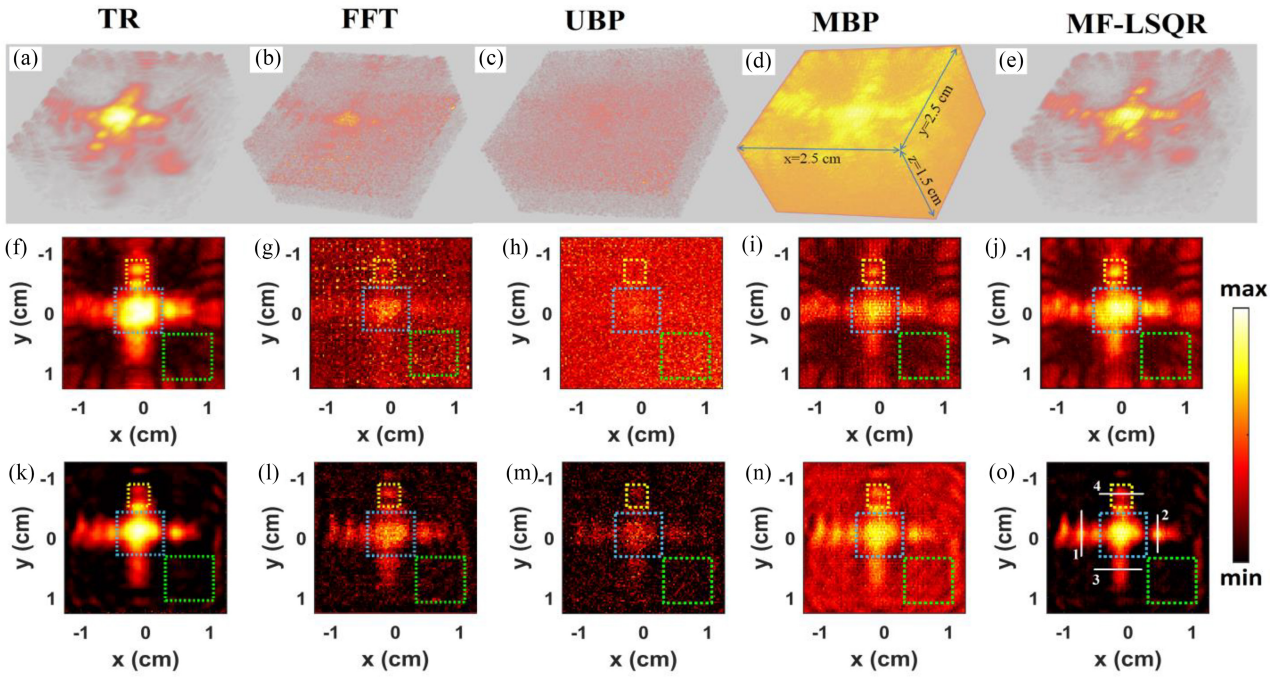

Fig. 7. XACT experimental results: (a)–(e) 3-D view, (f)–(j) MIP, and (k)–(o) reconstruction slice (at a plane 3.5-cm away from the detection grid) from the TR, FFT-based, UBP, MBP, and MF-LSQR reconstructions, respectively.

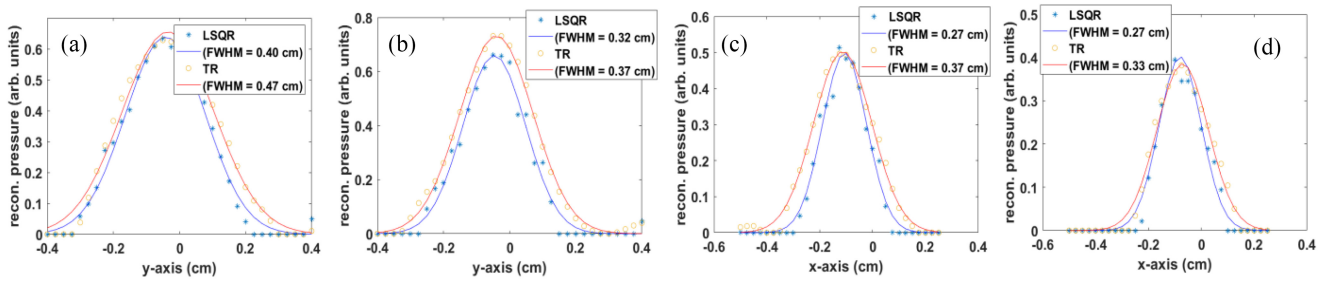

Fig. 8. Cross-sectional profile plots of the LSQR and TR reconstruction along (a) line 1 (b) line 2 (c) line 3, and (d) line 4 shown in Fig. 7(o). The FWHM of the profiles (given in each figure legend) were obtained by Gaussian fitting the reconstructed profiles.

Moreover, the TR takes about thrice as much time as the MF-LSQR does. In order to take higher frequency components into account, the spatial grid size (h) for TR needs to be decreased accordingly which will further increase the computation time. The Laplacian regularization has noise ameliorating capability and hence the MFLSQR reconstruction yields good CNRs for the chosen regions without compromising the resolution of the reconstructed structures.

The electromagnetic interference in the DAQ is the main source of the noise in the XA signals. Additionally, the reflections of the head wave and the XA waves between the phantom and detection array and inaccuracy in the co-ordinates of the elements in the planar detection grid also contribute to the artifacts in the XACT reconstructions.

V. Conclusion

MB algorithms were employed for evaluating 3-D XACT reconstructions and their efficacy was demonstrated on numerical and experimental datasets. Unlike the traditional MB algorithms which require explicit computation and storage of the measurement-matrix (**M**), the algorithm used (MF-LSQR) employs routines for on-the-fly evaluation of $\{\mathbf{M}\underline{u}, \mathbf{M}^{\mathbf{T}}\underline{v}\}$ to solve the Laplacian-regularized LS problems, thus reducing the computation times and memory costs corresponding to the evaluation and storage of **M**. Algorithm for evaluating noniterative MBP reconstruction is also provided. The MB schemes were used to evaluate the reconstructions for numerical and experimental XACT datasets which were compared with the traditional UBP, FFT-based, and TR reconstructions. Due to the regularization, MB algorithms were able to ameliorate the noisy artifacts, while the structures in UBP and FFT-based reconstructions were overshadowed by the noisy artifacts. The difference between the performance of MB and the traditional UBP and FFT-based algorithms is even more evident in the experimental XACT reconstructions, where the target is clearly visible in the MB reconstructions, while it is barely discernible in the UBP reconstruction and the FFT-based algorithm performing marginally better than the UBP.

The TR restricts frequency components higher than the maximum frequency supported by the grid spacing used for wave propagation which leads to reduced noise in the reconstructions. Therefore, TR yields the best CNRs for the

experimental XACT. However, it also leads to the loss of information of the sharp structures and edges of the target which are encoded in the high-frequency components thus the resolution is adversely affected. We found out that the FWHMs of TR reconstructions were ∼15%–35% larger than the MF-LSQR counterparts. The TR is based upon wave-propagation at each time step, and hence the evaluation of TR reconstruction takes much longer than the FFT, UBP, and MBP algorithms. For evaluating the experimental reconstructions, TR took about thrice as much time as the iterative MF-LSQR did. In order to take higher frequency components into account, the spatial grid spacing (h) for TR needs to be decreased accordingly which will further increase the computation time. Moreover, the simulation results also demonstrate that TR is more susceptible to the limited view problem and low detector density. The iterative MF-LSQR performed the best across all the test cases due to the superior noise suppression by the Laplacian regularizer without compromising the resolution of the reconstructed structures.

To the best of our knowledge, the results shown in this article are the first demonstration of the MB 3-D XACT. The computational efficiency of the proposed MB algorithms is governed by the functions for $\{\mathbf{M}\underline{u}, \mathbf{M}^{\mathbf{T}}\underline{v}\}$ computations. Work is ongoing to accelerate these functions using GPUs in order to facilitate high-resolution/real-time/large-scale XACT imaging. Unlike the conventional reconstruction algorithms, such as UBP, FFT-based, and TR, MB algorithms can facilitate incorporating experimental attributes, such as acoustic heterogeneity distribution, finite detector aperture, etc. Integrating such attributes in the MB algorithms will be the focus of the future research, which we believe is the right step toward the clinical translation of XACT.

ACKNOWLEDGMENT

All the authors declare that they have no known conflicts of interest in terms of competing financial interests or personal relationships that could have an influence or are relevant to the work reported in this article.

REFERENCES

[1] J. M. Boone, A. L. C. Kwan, K. Yang, G. W. Burkett, K. K. Lindfors, and T. R. Nelson, "Computed tomography for imaging the breast," *J. Mammary Gland Biol. Neoplasia*, vol. 11, no. 2, pp. 103–111, Apr. 2006.

[2] A. Momose, T. Takeda, Y. Itai, and K. Hirano, "Phase–contrast X–ray computed tomography for observing biological soft tissues," *Nat. Med.*, vol. 2, no. 4, pp. 473–475, Apr. 1996.

[3] W. A. Kalender, "X-ray computed tomography," *Phys. Med. Biol.*, vol. 51, no. 13, p. R29, Jun. 2006.

[4] L. W. Brady and C. A. Perez, *Perez & Brady's Principles and Practice of Radiation Oncology*. Philadelphia, PA, USA: Lippincott Williams Wilkins, May 2013.

[5] E. B. Podgorsak and K. Kainz, *Radiation Oncology Physics: A Handbook for Teachers and Students*, Int. Atom. Energy Agency, Vienna, Austria, May 2003.

[6] C. B. Dracham, A. Shankar, and R. Madan, "Radiation induced secondary malignancies: A review article," *Radiat. Oncolo. J.*, vol. 36, no. 2, pp. 85–94, Jun. 2018.

[7] L. Xiang, B. Han, C. Carpenter, G. Pratx, Y. Kuang, and L. Xing, "X-ray acoustic computed tomography with pulsed x-ray beam from a medical linear accelerator," *Med. Phys.*, vol. 40, no. 1, Jan. 2013, Art. no. 10701.

[8] E. Robertson and L. Xiang, "Theranostics with radiation-induced ultrasound emission (TRUE)," *J. Innovat. Opt. Health Sci.*, vol. 11, no. 3, May 2018, Art. no. 1830002.

[9] P. Samant, L. Trevisi, X. Ji, and L. Xiang, "X-ray induced acoustic computed tomography," *Photoacoustics*, vol. 19, Sep. 2020, Art. no. 100177.

[10] S. Wang, "Radiation-induced acoustic imaging system development and applications," M.S. thesis, School Comput. Electr. Eng., Univ. Oklahoma, Norman, OK, USA, 2019.

[11] S. Hickling, M. Hobson, and I. E. Naqa, "Feasibility of X-ray acoustic computed tomography as a tool for noninvasive volumetric in vivo dosimetry," *Int. J. Radiat. Oncol. Biol. Phys.*, vol. 90, no. 1, p. S843, Sep. 2014.

[12] C. H. Kim et al., " Water dosimetry device using x-ray induced ultrasonic waves," U.S. Patent 16 488 236, Dec. 19, 2019.

[13] L. Xiang, S. Tang, M. Ahmad, and L. Xing, "High resolution X-ray-induced acoustic tomography," *Sci. Rep.*, vol. 6, May 2016, Art. no. 26118.

[14] S. Tang, K. Yang, Y. Chen, and L. Xiang, "X-ray-induced acoustic computed tomography for 3D breast imaging: A simulation study," *Med. Phys.*, vol. 45, no. 4, pp. 1662–1672, Apr. 2018.

[15] H. Shirato et al., "Feasibility of insertion/implantation of 2.0-mm-diameter gold internal fiducial markers for precise setup and real-time tumor tracking in radiotherapy," *Int. J. Radiat. Oncol. Biol. Phys.*, vol. 56, no. 1, pp. 240–247, 2003.

[16] E. Robertson, P. Samant, S. Wang, T. Tran, X. Ji, and L. Xiang, "X-ray-induced acoustic computed tomography (XACT): Initial Experiment on bone sample," *IEEE Trans. Ultrason., Ferroelectr., Freq. Control*, vol. 68, no. 4, pp. 1073–1080, Apr. 2021.

[17] S. Choi, E.-Y. Park, S. Park, J. H. Kim, and C. Kim, "Synchrotron X-ray induced acoustic imaging," *Sci. Rep.*, vol. 11, no. 1, p. 4047, 2021.

[18] S. Wang, V. Ivanov, P. K. Pandey, and L. Xiang, "X-ray-induced acoustic computed tomography (XACT) imaging with single-shot nanosecond x-ray," *Appl. Phys. Lett.*, vol. 119, no. 18, 2021, Art. no. 183702.

[19] S. Choi et al., "In situ X-ray-induced acoustic computed tomography with a contrast agent: A proof of concept," *Opt. Lett.*, vol. 47, no. 1 pp. 90–93, 2022.

[20] F. Forghani et al., "Simulation of x-ray-induced acoustic imaging for absolute dosimetry: Accuracy of image reconstruction methods," *Med. Phys.*, vol. 47, no. 3, pp. 1280–1290, Dec. 2019.

[21] S. Hickling, P. Léger, and I. E. Naqa, "On the detectability of acoustic waves induced following irradiation by a radiotherapy linear accelerator," *IEEE Trans. Ultrason., Ferroelectr., Freq. Control*, vol. 63, no. 5, pp. 683–690, May 2016.

[22] Y. Zheng et al., "X-ray-induced acoustic computed tomography for guiding prone stereotactic partial breast irradiation: A simulation study," *Med. Phys.*, vol. 47, no. 9, pp. 4386–4395, May 2020.

[23] M. Wang et al., "Towards in vivo dosimetry for prostate radiotherapy with a transperineal ultrasound array: A simulation study," *IEEE Trans. Radiat. Plasma Med. Sci.*, vol. 5, no. 3, pp. 373–382, May 2021.

[24] S. Hickling, H. Lei, M. Hobson, P. Léger, X. Wang, and I. El Naqa, "Experimental evaluation of x-ray acoustic computed tomography for radiotherapy dosimetry applications," *Med. Phys.*, vol. 44, no. 2, pp. 608–617, Feb. 2017.

[25] S. Hickling, M. Hobson, and I. E. Naqa, "Characterization of X-ray acoustic computed tomography for applications in radiotherapy dosimetry," *IEEE Trans. Radiat. Plasma Med. Sci.*, vol. 2, no. 4, pp. 337–344, Jul. 2018.

[26] H. Lei et al., "Toward in vivo dosimetry in external beam radiotherapy using X-ray acoustic computed tomography: A soft-tissue phantom study validation," *Med. Phys.*, vol. 45, no. 9, pp. 4191–4200, Sep. 2018.

[27] J. Kim et al., "X-ray acoustic-based dosimetry using a focused ultrasound transducer and a medical linear accelerator," *IEEE Trans. Radiat. Plasma Med. Sci.*, vol. 1, no. 6, pp. 534–540, Nov. 2017.

[28] M. Xu and L. V. Wang, "Universal back-projection algorithm for photoacoustic computed tomography," *Phys. Rev. E, Stat. Phys. Plasmas Fluids Relat. Interdiscip. Top.*, vol. 71, no. 1, Jan. 2005, Art. no. 016706.

[29] P. K. Pandey et al, "Model-based X-ray-induced acoustic computed tomography," *IEEE Trans. Ultrason., Ferroelectr., Freq. Control*, vol. 68, no. 12, pp. 3560–3569, Dec. 2021.

[30] P. K. Pandey, H. Om Aggrawal, S. Wang, K. Kim, A. Liu, and L. Xiang, "Ring artifacts removal in X-ray-induced acoustic computed tomography," *J. Innovat. Opt. Health Sci.*, vol. 15 no. 3, 2022, Art. no. 2250017.

[31] B. E. Treeby and B. T. Cox, "K-Wave: MATLAB toolbox for the simulation and reconstruction of photoacoustic wave fields," *J. Biomed. Opt.*, vol. 15, no. 2, Mar 2010, Art. no. 21314.

[32] "Tissue properties, speed of sound." IT'IS Foundation. Accessed: Sep. 25, 2022. [Online]. Available: https://itis.swiss/virtual-population/tissue-properties/database/acoustic-properties/speed-of-sound/
[33] J. Poudel, Y. Lou, and M. A. Anastasio, "A survey of computational frameworks for solving the acoustic inverse problem in three-dimensional photoacoustic computed tomography," *Phys. Med. Biol.*, vol. 64, no. 14, 2019, Art. no. 14TR01.
[34] G. Paltauf, J. A. Viator, S. A. Prahl, and S. L. Jacques, "Iterative reconstruction algorithm for optoacoustic imaging," *J. Acoust. Soc. America*, vol. 112, no. 4, pp. 1536–1544, 2002.
[35] P. Ephrat, "Three-dimensional photoacoustic imaging by sparse-array detection and iterative image reconstruction," *J. Biomed. Opt.*, vol. 13, no. 5, 2008, Art. no. 54052.
[36] K. Wang, R. W. Schoonover, R. Su, A. Oraevsky, and M. A. Anastasio, "Discrete imaging models for three-dimensional optoacoustic tomography using radially symmetric expansion functions," *IEEE Trans. Med. Imag.*, vol. 33, no. 5, pp. 1180–1193, May 2014.
[37] J. Zhang et al., "Effects of different imaging models on least-squares image reconstruction accuracy in photoacoustic tomography," *IEEE Trans. Med. Imag.*, vol. 28, no. 11, pp. 1781–1790, Nov. 2009.
[38] X. L. Deán-Ben, A. Buehler, V. Ntziachristos, and D. Razansky, "Accurate model-based reconstruction algorithm for three-dimensional optoacoustic tomography," *IEEE Trans. Med. Imag.*, vol. 31, no. 10, pp. 1922–1928, Oct. 2012.
[39] K. Wang, C. Huang, Y.-J. Kao, C.-Y. Chou, A. A. Oraevsky, and M. A. Anastasio, "Accelerating image reconstruction in three-dimensional optoacoustic tomography on graphics processing units," *Med. Phys.*, vol. 40, no. 2, 2013, Art. no. 23301.
[40] L. Ding, D. Razansky, and X. L. Dean-Ben, "Efficient 3-D model-based reconstruction scheme for arbitrary optoacoustic acquisition geometries," *IEEE Trans. Med. Imag.*, vol. 36, no. 9, pp. 1858–1867, Sep. 2017.
[41] P. K. Pandey, S. Wang, and L. Xiang, "Model based reconstruction algorithm for x-ray induced acoustic tomography," in *Proc. SPIE Med. Imag. Phys.*, Feb. 2021, Art. no. 115953V.
[42] L. Ding, D. Razansky, and X. L. Dean-Ben, "Model-based reconstruction of large three-dimensional optoacoustic datasets," *IEEE Trans. Med. Imag.*, vol. 36, no. 9, pp. 2931–2940, Sep. 2020.
[43] A. Buehler et al., "Model-based optoacoustic inversions with incomplete projection data," *Med. Phys.*, vol. 38, no. 3, pp. 1694–1704, Mar. 2011.
[44] A. Klose, "Optical tomography based on the equation of radiative transfer," M.S. thesis, Dept. Phys., Freie Universitat, Berlin, Germany, 2002.
[45] P. C. Hansen, "Regularization tools: A MATLAB package for analysis and solution of discrete ill-posed problems," *Numer. Algorithms*, vol. 6, no. 1, pp. 1–35, 1994.
[46] L. Ding, X. Deán-Ben, C. Lutzweiler, D. Razansky, and V. Ntziachristos, "Image reconstruction in cross-sectional optoacoustic tomography based on non-negative constrained model-based inversion," in *Proc. Eur. Conf. Biomed. Opt. Opt. Soc. America*, 2015, Art. no. 953919.